Carbohydrate Polymers 117 (2015) 616–623

Contents lists available at ScienceDirect

Carbohydrate Polymers

journal homepage: www.elsevier.com/locate/carbpol

Effects of surface functionalized graphene oxide on the behavior of sodium alginate

Ling Nie, Changhua Liu*, Jia Wang, Ying Shuai, Xiaoyan Cui, Li Liu

College of Chemistry and Chemical Engineering, Southwest University, Chongqing 400715, PR China

ARTICLE INFO

Article history:
Received 20 May 2014
Received in revised form 10 August 2014
Accepted 22 August 2014
Available online 16 September 2014

Keywords:
Graphene oxide
Modified graphene oxide
Biocomposite
Interaction

ABSTRACT

The aim of this study was to improve the miscibility between fillers and polymer through modifying the face of graphene oxide (*GO*). In order to compare the effects of *GO* and modified graphene oxide (*MGO*) to sodium alginate (*SA*), sodium alginate/graphene oxide (*SA/GO-n*) and sodium alginate/modified graphene oxide (*SA/MGO-n*) biocomposite films were prepared, then the interaction between nanofillers and matrix was evaluated. The structure, morphologies and properties of biocomposites were characterized by Fourier transform infrared (*FTIR*) spectroscopy, X-ray diffraction (*XRD*), thermal gravimetric analysis (*TGA*), Ultraviolet–visible (*UV–vis*), scanning electron microscopy (*SEM*) and mechanical tests. The results revealed that strong interactions existed between *GO* (*MGO*) and *SA*. Compared with neat *SA* film, the maximum level of Young's moduli (E), tensile strength (σ_b) and elongation at break (ε_b) of the *SA/MGO* biocomposites improved by 37.8%, 68.4% and 44.9%, while that of the *SA/GO* biocomposites improved by 19.6%, 44% and 36.5%.

1. Introduction

Sodium alginate (*SA*) is a very important biodegradable material, which is widely used in the fields of drug release, packaging material, agriculture, tissue engineering and biological studies due to its unique colloidal properties include thickening, stabilizing, suspending, film forming, gel producing and emulsion stabilizing forming (Augst, Kong, & Mooney, 2006; Fayaz, Balaji, Girilal, Kalaichelvan, & Venkatesan, 2009; Kawaguchi et al., 2006; Rhim, 2004; Wang, Liu, Shuai, Cui, & Nie, 2014). However, compared with conventional polymers, neat *SA* exhibits many disadvantages, such as strong hydrophilic character, poor mechanical properties and low thermal stability (Alboofetileh, Rezaei, Hosseini, & Abdollahi, 2013; Sharma, Sanpui, Chattopadhyay, & Ghosh, 2012), which greatly restrict its applications. Thus, an effective approach for improving the situation is needed. One significant strategy is to fill inorganic or organic nanoparticles into *SA* matrix to overcome its disadvantages (Coleman et al., 2004; Usuki, Hasegawa, & Kato, 2005).

Among various nanofillers, graphene, a single-atom-thick sheet of sp^2-hybridized carbon atoms (Ma, Chang, Zheng, & Ma, 2013; Park and Ruoff, 2009), has been attracted a great deal of attention in recent years owning to its low-cost, exceptional electron transport, high surface area and mechanical properties (Kim, Abdala, & Macosko, 2010; Zhong, Huang, Yang, & Cheng, 2011). However, it is difficult to obtain a good dispersion in polymer matrixes, resulting in serious phase separation and worse interfacial adhesion (Yuan, Zou, Liao, & Dai, 2012; Wang, Jin, & Song, 2012). In order to improve the dispersion and gain well interfacial interaction between nanofillers and matrix, oxide method was used to prepare derivatized graphene with oxygen containing functional groups on their basal planes and edges, such as hydroxyl, epoxide, carbonyl and carboxylic acid (Suhas, Raghu, Jeong, & Aminabhavi, 2013). These functional groups make it completely exfoliated to produce aqueous colloidal suspensions of graphene oxide sheets by sonication (Qiu et al., 2011; Rafiee et al., 2009), and improve the interaction with polymer chains to produce strong interfacial interaction by hydrogen bonds or electrostatic interaction. For graphene oxide, the hydroxyl and carboxyl groups can react with special group reagents to produce a promising modified filler to improve the properties of polymer/*GO* composites. For instance, the epoxy and carboxyl groups in graphene oxide favor to react with primary amine group by addition to modify graphene oxide (*MGO*) (Dreyer, Park, Bielawski, & Ruoff, 2010; Han, Yan, Chen, & Li, 2011). In addition, some researchers have reported that the thermal stability, electrical and mechanical properties of polymers could be improved by the incorporation of *MGO* nanosheets which was modified by aromatic amines (Fang et al., 2010), however, it

* Corresponding author. Tel.: +86 2368252360; fax: +86 2368254000.
E-mail addresses: zhulin19@swu.edu.cn (L. Nie), chliu@swu.edu.cn (C. Liu), yuepangxin@sina.com (J. Wang), shuaiying314@sina.com (Y. Shuai), xycui@swu.edu.cn (X. Cui), ll330@swu.edu.cn (L. Liu).

http://dx.doi.org/10.1016/j.carbpol.2014.08.104
0144-8617/

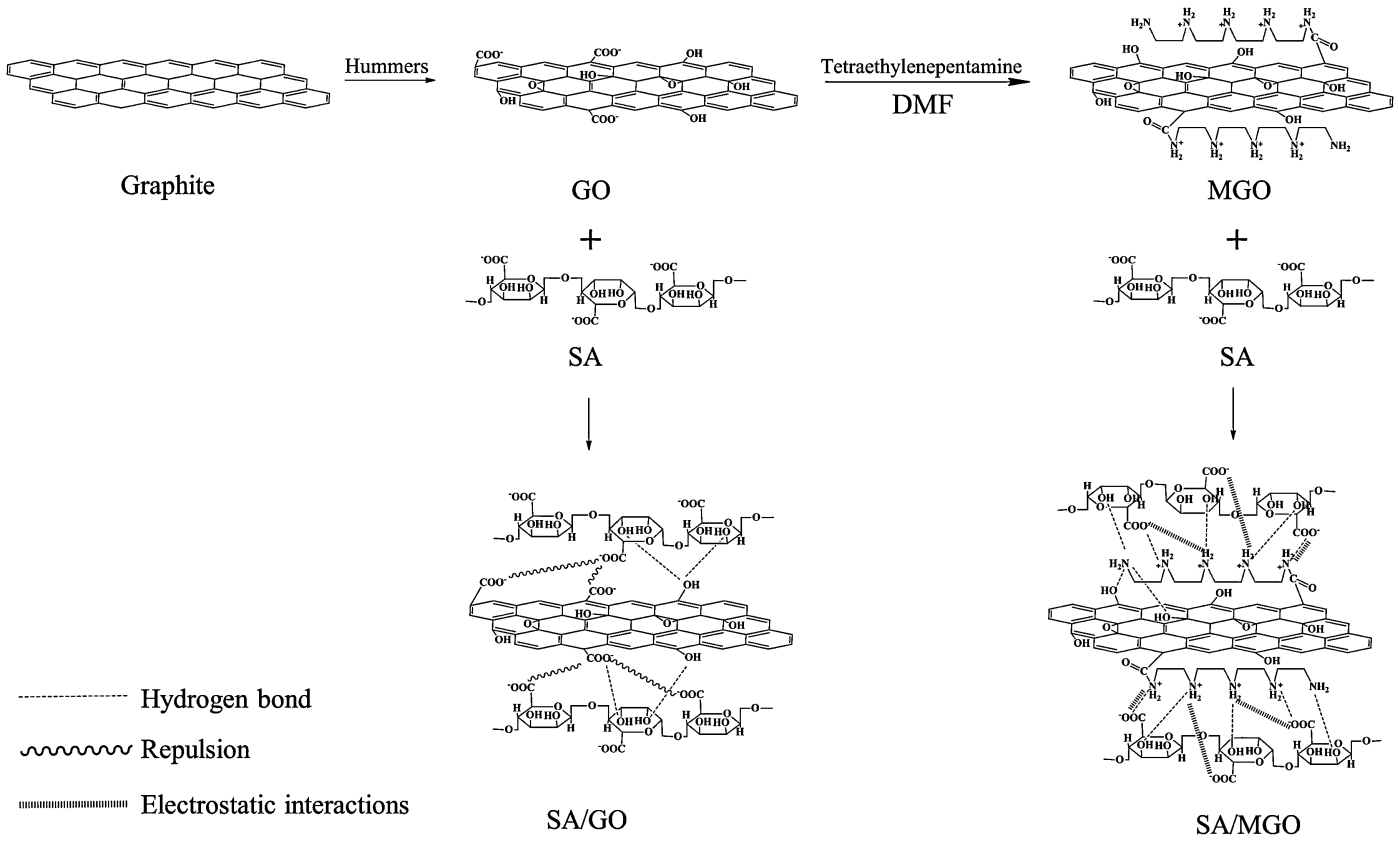

Scheme 1. Preparation routes of *MGO*, *SA*/*GO* and *SA*/*MGO-n* biocomposites, and schematic diagram of interaction between *SA* and fillers.

produced stronger steric hindrance and gain too little active site of amino group to effectively enhance the interfacial interactions. To overcome these problems, we chose tetraethylenepentamine to modified *GO* in that tetraethylenepentamine has a lot of nitrogen active site which can reduce the mutual repulsion between the dissociative COO^- groups of SA. Moreover, the nitrogen containing functional groups of *MGO* can be protonated to become multivalent nanoparticle, then readily form electrostatic interactions with negative charges $-COO^-$ groups on sodium alginate chains (Zhong et al., 2011), which can improve the compatibility with the matrix. Therefore, *MGO* can form much stronger electrostatic interactions and hydrogen bonds with the matrix (Scheme 1). Then the mechanical properties of *SA* biocomposites can be enhanced by the incorporation of *MGO* moieties into *SA* biocomposites.

In this work, we synthesized *MGO* using tetraethylenepentamine and prepared a series of *SA*/*GO-n* and *SA*/*MGO-n* biocomposite films, and studied the influence of *GO* and *MGO* loading on the morphologic, thermal stability, mechanical properties and moisture uptake of films. The biocomposites were analyzed by Fourier transform infrared (*FTIR*), X-ray diffraction (*XRD*), scanning electron microscopy (*SEM*), thermal gravimetric analysis (*TGA*) and tensile tests. The fundamental structure–property relationship of *GO*-based and *MGO*-based sodium alginate biocomposites were also discussed.

2. Experimental details

2.1. Materials

SA (chemical grade, viscosity: 1% solution, 25 °C, 200 ± 20 MPa s) was purchased from Taixing Chemical Company (Chongqing, China) and used without further purification. Graphite powder was supplied by Shanghai Huayi Group Hua Yuan Chemical Company Limited (Shanghai, China). Hydrogen peroxide 30% (H_2O_2, 30%) was supplied by Chengdu Kelong Chemical Reagent Company (Chengdu, China). Sulfuric acid (H_2SO_4, 98% v/v) and hydrochloric acid were purchased from Chongqing Chuandong Chemical Reagent Factory (Chongqing, China). Others were purchased from Taixing Chemical Company (Chongqing, China) The water used was distilled and deionized.

2.2. Preparation of GO

GO was prepared by oxidation of natural graphite powder according to the well-known Hummers method (Hummers & Offeman, 1958). Briefly, 2 g graphite powder and 120 mL H_2SO_4 were mixed in the beaker under stirring in an ice-bath. Next, 15 g $KMnO_4$ was added slowly into the beaker under stirring and the temperature was controlled below 20 °C. Then the ice-bath was removed and the system was kept for 2 h at 35 °C. Subsequently, 250 mL water and 10 mL 30% H_2O_2 were added slowly, respectively, and the mixture was stirred for another 2 h, resulting in a yellow-brown mixture. Finally, the resulting product was collected by centrifugation and washed with hydrochloric acid solution and water until the pH value of the upper layer suspension near 7. Graphene oxide powder was obtained under vacuum for 48 h at 50 °C.

2.3. Preparation of MGO

Two gram *GO* was dispersed into 200 mL N, N-dimethylformamide and sonicated in an ultrasonic bath for 4 h. Subsequently, 5 g dicyclohexylcarbodiimide and 30 g tetraethylenepentamine were added, respectively. Then the mixture was treated with ultrasound for 10 min and kept at 120 °C with stirring for 48 h to get a homogeneous dispersion.

Finally, the mixture was centrifuged and washed with alcohol and deionized water, respectively. The dried *MGO* (the weight ratio of tetraethylenepentamine to GO is approximately 0.15) was obtained at 60 °C overnight.

2.4. Preparation of SA/GO-n and SA/MGO-n biocomposite films

GO was suspended in 75 mL water using ultrasonication for 5 h. Then, *SA* was added to the suspension. In order to estimate the interaction between *GO* and *SA*, a series of different loading levels (0, 0.2, 0.5, 1.0, 1.5 and 2.0 wt%) of *SA/GO* mixture based on *SA* were prepared following by being heated at 60 °C for 4.5 h with constant stirring, pouring into a glass plate and being heated at 50 °C to obtain dry films after degassing under vacuum. A series of biocomposite films were coded as *SA*, *SA/GO-1*, *SA/GO-2*, *SA/GO-3*, *SA/GO-4* and *SA/GO-5*. The *SA/MGO-n* biocomposite films were prepared according to the same procedure and coded as *SA/MGO-1*, *SA/MGO-2*, *SA/MGO-3*, *SA/MGO-4* and *SA/MGO-5*, where the number *n* represented the different *GO* or *MGO* loadings. Dried films were conditioned at 40% RH and room temperature prior to testing.

2.5. Characterization of the biocomposite films

Fourier transform infrared (*FTIR*) spectra of *GO* and films were recorded on a Nicolet (Madison, WI, USA) 170SX Fourier transform infrared spectrometer in the wavelength range of 4000–500 cm^{-1} in the attenuated total reflection mode.

For transmission electron microscopy (*TEM*) researching, the suspension of *GO* and *MGO* were dropped onto copper grid individually which was coated with a carbon film and dried in a vacuum drying oven for 3 h, after that, the samples were examined using a JEM-2100 TEM (JEOL, Tokyo, Japan). Atomic force microscopy (*AFM*) images of *GO* and *MGO* were taken in the tapping mode by carrying out on MFP-3D-SA (Asylum Research, USA). The AFM samples were dispersion onto mico plates.

X-ray diffractometer (*XRD*) patterns of the samples were recorded on an X-ray diffractometer (XRD-3D, PuXi, Beijing, China) at a voltage of 36 kV and a current of 20 mA using Cu *Kα* radiation (λ = 0.154 nm). The scanning rate was 4°/min and the scanning range of 2*θ* was 5–40° at room temperature.

Mechanical test was performed using a Microelectronics Universal Testing Instrument Model Sans 6500 (Shenzhen, China) with the cross-head speed was 10 mm/min at room temperature and the initial grip separation was set at 50 mm. All of the test specimens were cut into 10 cm in length and 1 cm in width, and the samples were equilibrated at 43% relative humidity. For each sample, at least three replicates were tested, and the average value was regarded as the representative value.

The scanning electron microscopy (*SEM*) images of the films were obtained using a QuantaFEG450 SEM instrument (FEI, USA).

The Ultraviolet–visible absorption (*UV–vis*) spectra of different contents of *SA/GO-n* and *SA/MGO-n* biocomposites were recorded from 200 to 700 nm using a *UV–vis* spectrophotometer 2550 (Suzhou, China). The *UV–vis* spectrums of the biocomposites were recorded using a blank cuvette as reference.

Thermogravimetric analysis (*TGA*) of *SA/GO-n* and *SA/MGO-n* biocomposites were carried out on a TA-STDQ600 (New Castle, USA) thermogravimetric analyzer with a heating rate of 10 °C/min under a dynamic dry nitrogen flow of 20 mL/min. An empty pan was used as a reference.

Triplicate samples of each film were weighed by using a weighing balance. Before test, the samples were cut into thin rectangular strips with dimensions of 50 × 10 × 0.1 mm^3 and dried overnight at 80 °C. Then they were conditioned at 92% RH ($CuSO_4$ saturated solution) for 5 days to ensure equilibrium of moisture before testing. The % uptake was determined by the following equation:

$$\text{Mu}\ (\%) = \frac{W_{\text{wet}} - W_{\text{dry}}}{W_{\text{dry}}} \times 100$$

where W_{wet} and W_{dry} are the weights of the wet and dry films, respectively.

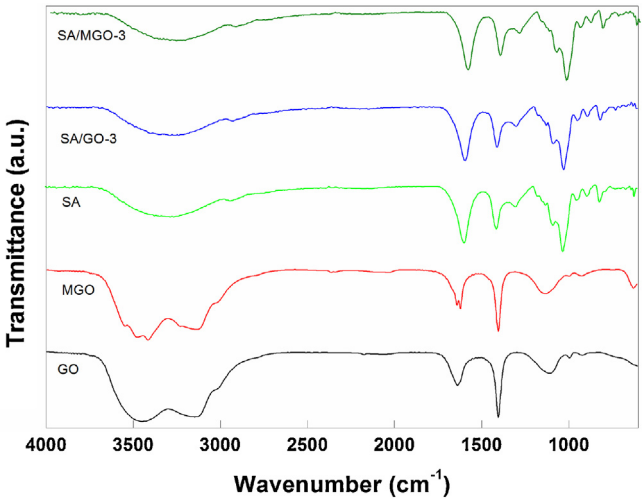

Fig. 1. *FT-IR* spectra of *GO*, *MGO*, *SA/GO-3* and *SA/MGO-3* biocomposite films.

3. Results and discussion

3.1. FTIR spectra analysis

The *FTIR* spectra of *SA/GO-3* and *SA/MGO-3* exhibited in Fig. 1 with *GO* and *MGO* powder. For the *GO* spectrum, charateristic peaks appeared at 3414, 1638, 1618, 1400 and 1126 cm^{-1} were assigned to OH stretching vibration, C=O stretching vibration of the carboxylic group, C=C stretching vibration corresponding to the remaining sp^2 character, C—OH stretching vibration of the carboxylic group and C—O stretching vibration, respectively. The characteristic spectrum of *GO* proved the successful oxidation of graphite to *GO*. For the *MGO* spectrum, the peaks at 3446, 3144, 1635, 1400 and 1103 cm^{-1} were attributed to N—H stretching vibration of the amino groups, C—H bending vibration, C=O stretching vibration of the amide groups, C—N stretching vibration, C—OH stretching vibration (Sha, Xie, Ma, Dong, & Wang, 2011). These main characteristic peaks indicated that *MGO* has been successfully prepared. The spectrum peak at 3355 and 3132 cm^{-1} of neat *SA* film could be attributed to OH stretching vibration and C—H stretching vibration, the bands at 1593 and 1407 cm^{-1} correspond to symmetric and asymmetric COO^- stretching vibration of carboxylate salt group, and the peak at 1026 cm^{-1} was assigned to the stretching vibration of C—O—C groups. When *GO* was added in *SA*, the peaks for *SA/GO-3* at 3355, 1593 cm^{-1} shifted to low wave-numbers 3331, 1591 cm^{-1}, which could be attributed to the interaction of *SA* and *GO* through intermolecular hydrogen bonds. However, the peak for *SA/MGO-3* at 3355, 1593 cm^{-1} shifted to lower wave-numbers 3272, 1590 cm^{-1}, it can be attributed that *MGO* possesses $-NH_2$ and —NH groups, leading to stronger interaction resulting from hydrogen bonds and electrostatic interactions between the *MGO* and the *SA*, which can result in an enhanced mechanical response.

3.2. TEM and AFM analysis

From Fig. 2, exfoliated *GO* (Fig. 2a) and *MGO* (Fig. 2b) nanosheets are clearly observed and they have been well exfoliated into

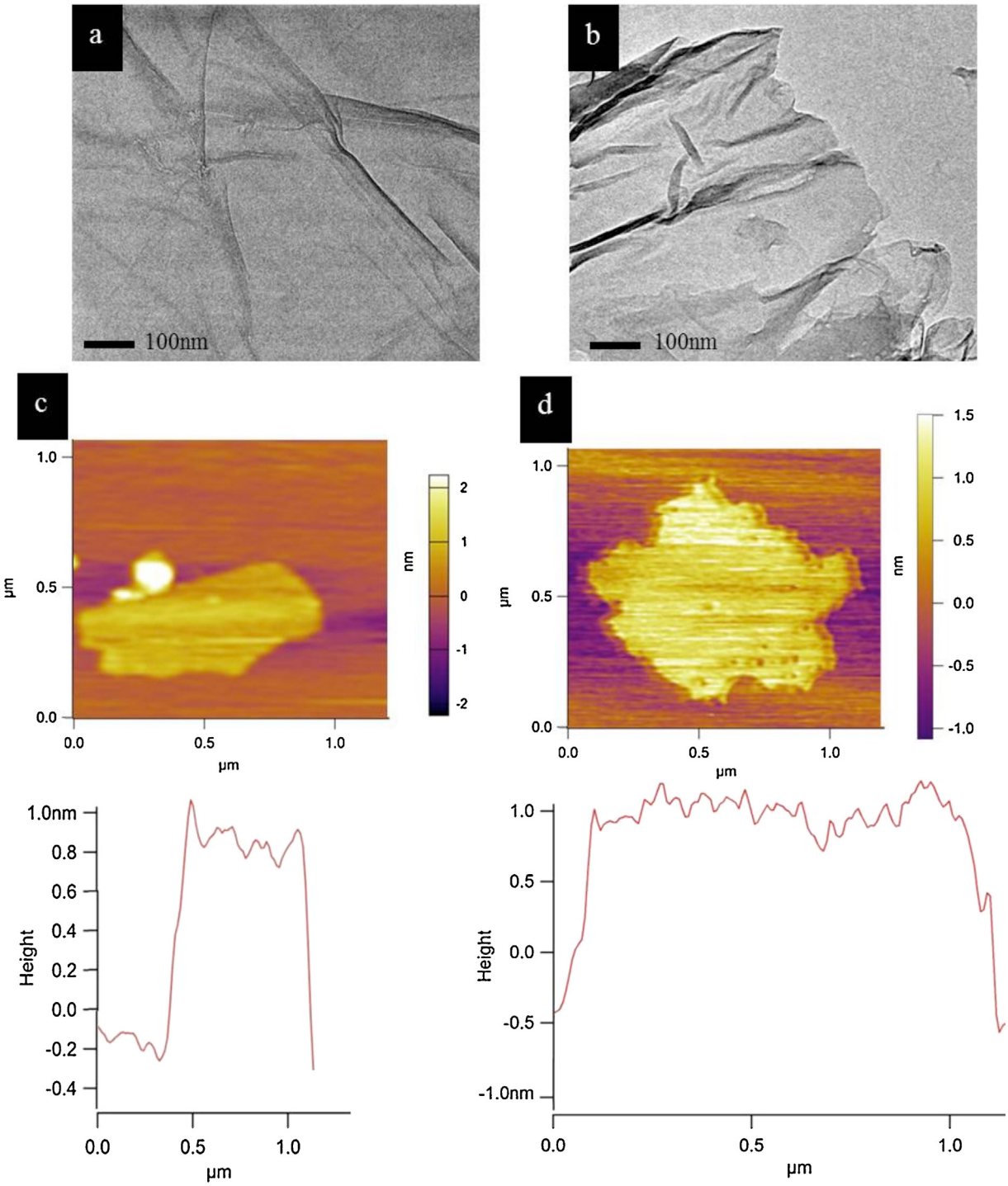

Fig. 2. TEM images of *GO* (a) and *MGO* (b); AFM images of *GO* (c) and (d) with their height profiles, respectively.

nanosheets. TEM image of *GO* displays a wrinkled laminar structure with ultrathin nanosheets. *TEM* image of *MGO* shows a similar wrinkled laminar structure that is much plumper than *GO* and that has abundant gaps between layers, and those phenomena may be attributed to the existence of the nitrogen containing functional groups of *MGO*. Fig. 2 presents the *AFM* image of *GO* (Fig. 2c) and *MGO* (Fig. 2d) sheets dispersed in water. It showed that the dimension of both *GO* and *MGO* sheets are about several hundred nanometres to several micrometres in length, and about 0.8 nm and 1.0 nm in thickness, respectively, suggesting a better exfoliation of *GO* and *MGO* in water. Thus, we could conclude that single and few-layer *GO* and *MGO* were obtained. In addition, the thickness of the obtained *MGO* sheet is thicker than that of the exfoliated *GO*, which is due to the graft of the nitrogen containing functional groups.

3.3. X-ray diffraction

The *XRD* patents of *GO*, *MGO* and biocomposite films with different loading of *GO* or *MGO* are shown in Fig. 3. It can be clearly seen from Fig. 3 that the amorphous structure of neat *SA* displayed a broad diffraction commencing from 23° to 27° in 2θ.

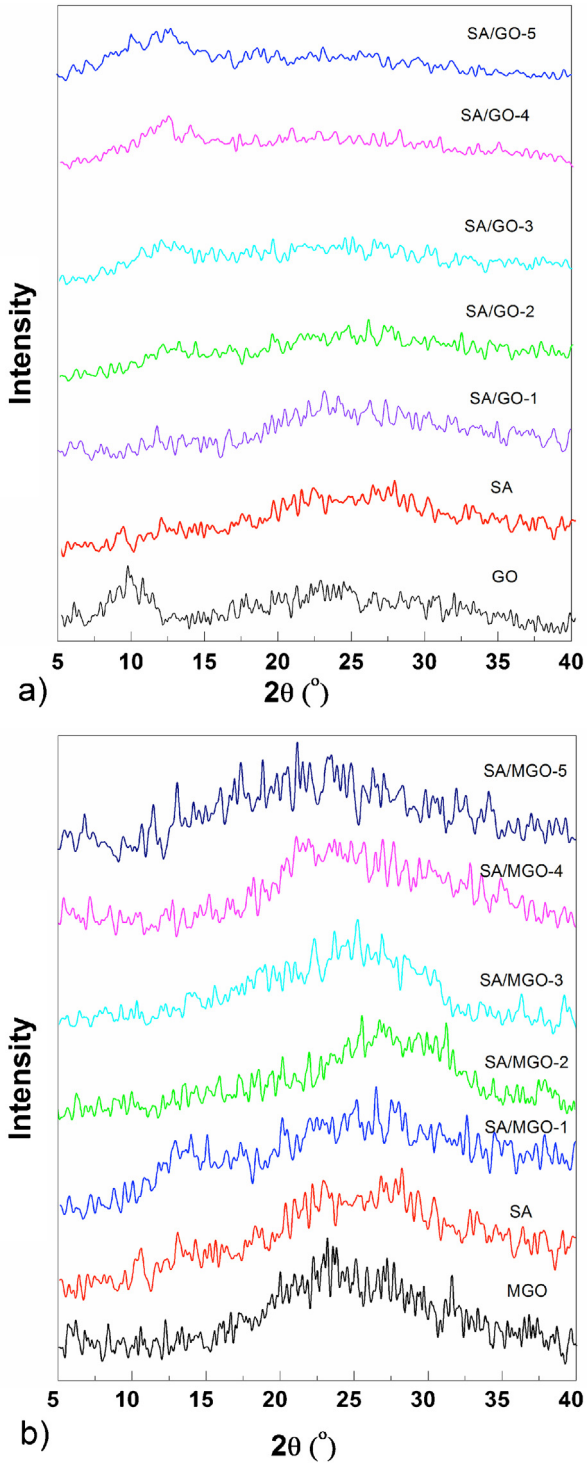

Fig. 3. *XRD* patterns of *SA* film, *SA/GO-n* (a) and *SA/MGO-n* (b) biocomposite films.

The *XRD* pattern of neat *GO* showed a strong peak at $2\theta = 10^{\circ}$, which indicated that *GO* possessed some crystallization. However, a broadened peak indicated amorphous *MGO* at about 24° was only found. After adding *GO*, the characteristic diffraction peak of *GO* was not observed in the biocomposite films, which indicated that it dispersed well in the *SA* matrix at low loading levels. However, the character diffraction peak of *GO* and *MGO*, with high loading content, appeared at $2\theta = 10^{\circ}$, 24° in the biocomposite films, which is the characterization pattern of *GO* and *MGO*. Combining to analysis of SEM, we can infer that this may be that higher loading of fillers resulted in aggregations during the processing. *MGO* came into aggregating with 2.0 wt% loading while *GO* came into aggregating with 1.5 wt% loading. Those revealed that the compatibility was improved after *GO* was modified. The results can be contributed that *MGO* possesses a lot of $-NH_2$ and $-NH$ groups and easily be protonated to produce a multivalent nanoparticle, which can produce a physical crosslink with *SA* through electrostatic interactions exception of hydrogen bonding interactions, leading to much stronger interactions between the *SA* and *MGO*.

3.4. Mechanical properties

To understand the effect of the functional groups on the basal plane of *GO* on the mechanical properties, we studied Young's moduli (E), tensile strength (σ_b) and elongation at break (ε_b) of the films with adjustable compositions. From Fig. 4, it was found that *GO* and *MGO* had an obvious reinforcing effect on the *SA* matrix. The tensile strength of *SA* (Fig. 4a) was only 41.16 MPa. For the *SA/GO-n* and *SA/MGO-n* biocomposites, the maximum of the tensile strength reached 59.28 MPa and 69.32 MPa (improved by 44% and 68.4%) respectively, indicating a considerable reinforcing effect from *GO* and *MGO* nanoparticles. However, it is clearly illustrated that further addition of *GO* or *MGO* could not considerably improve tensile strength. The tensile modulus values of biocomposite films (Fig. 4b) firstly increased with low level, and the maximum occurred at the 1.0 wt% *GO* or *MGO* loading. And the elongation at break values (Fig. 4c) show a reduction trend when the content of fillers is less than 1.0 wt% and reached a minimum of 5.93% or 5.15% at 1.0 wt% content, and then show an increase when the content of fillers is more than 1.0 wt%. These results suggested that *GO* and *MGO* could improve the strength and stiffness of *SA* films at the expense of flexibility, however, the functional *GO* (refers *MGO*) exhibited more prestige. The improvement in the mechanical properties was due to the good dispersion of *GO* or *MGO* within the *SA* matrix and the strong interfacial interactions between *GO* or *MGO* and *SA* matrix, and the good dispersion also restrained the slippage movement among *SA* molecules, thus adding a small amount of *GO* or *MGO* decreased elongation at break of *SA* films. While the amino groups of *MGO* have a lot of nitrogen active site and some of them can be protonated, which can reduce the mutual repulsion between the dissociative COO^- groups of *SA* and produce a stronger physical crosslink through electrostatic interactions exception of hydrogen bonding interaction. Thus, *SA/MGO-n* biocomposites have better mechanical properties than *SA/GO-n* biocomposites. While at higher contents of *GO* or *MGO*, the tensile strength of biocomposite films decreased abruptly, it was due to the agglomeration of nanoparticles which can weaken the interfacial interaction.

3.5. Thermal stability analysis

The thermal stability of the *SA* and their biocomposite films were studied by thermogravimetric analysis and differential thermogravimetry, and presented in Fig. 5, respectively. It could be noted basically two main thermal events. The first one before 100 °C was associated with the loss of absorbed water. The second stage of the weight loss in the temperature range of 200–300 °C corresponded to decomposition of *SA*. The summary of *TGA* results were listed in Table 1. It was found that all *SA/GO-n* and *SA/MGO-n* biocomposite films showed a higher decomposition temperature than neat *SA* film, however, the decomposition temperature of almost all *SA/MGO-n* biocomposite films was higher than that of *SA/GO-n* biocomposite films with the same loading. These results suggested that the mobility of *SA* chains was suppressed by strong hydrogen bonding interactions or electrostatic interactions with *GO* or *MGO*. Moreover, *MGO* possesses much more active groups than *GO*, which can produce a stronger interfacial interaction, hence,

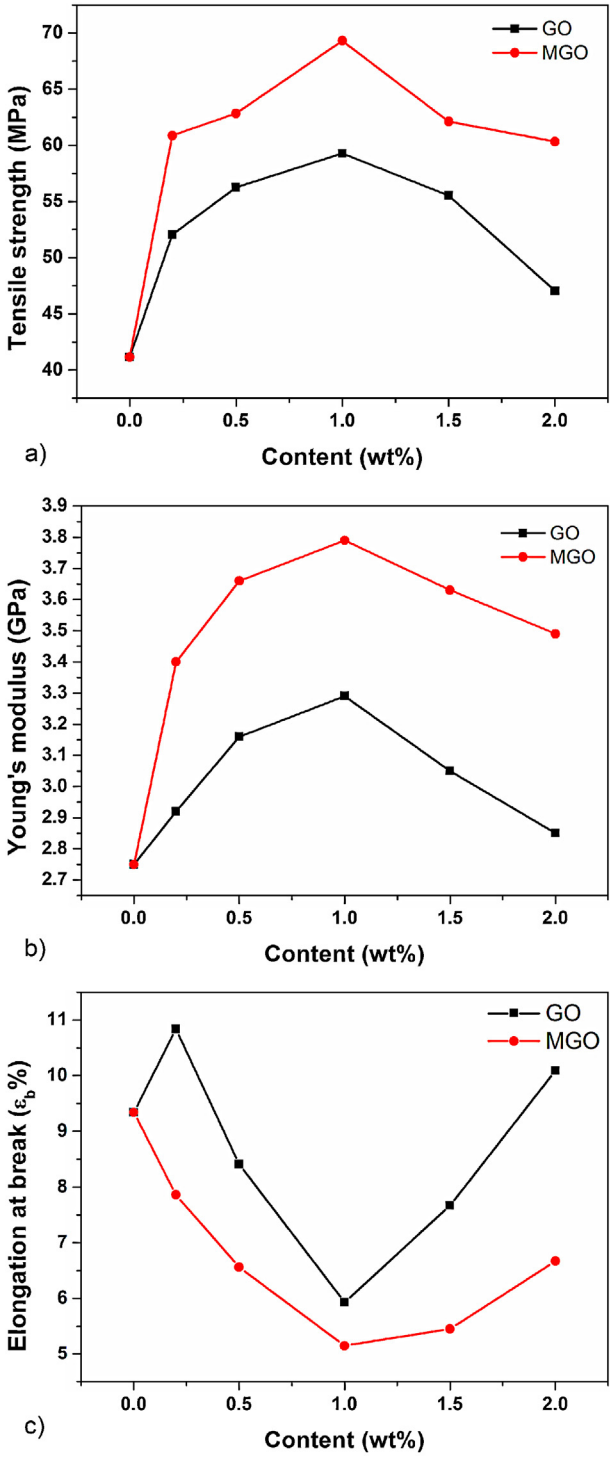

Fig. 4. Tensile strength (a), elongation at break (b) and Young's modulus (c) of *SA/GO-n* and *SA/MGO-n* biocomposite films.

SA/MGO-n biocomposites have better thermal stability than *SA/GO-n* biocomposites.

3.6. Scanning electron microscopy

SEM studies provided direct information regarding the interfacial interactions of biocomposite films, as shown in Fig. 6. The surface of neat *SA* (Fig. 6a) films displayed a generally smooth morphology. The fracture surface of *SA/GO-1* (Fig. 6b), *SA/GO-3* (Fig. 6d) showed some buckling, and no obvious agglomeration

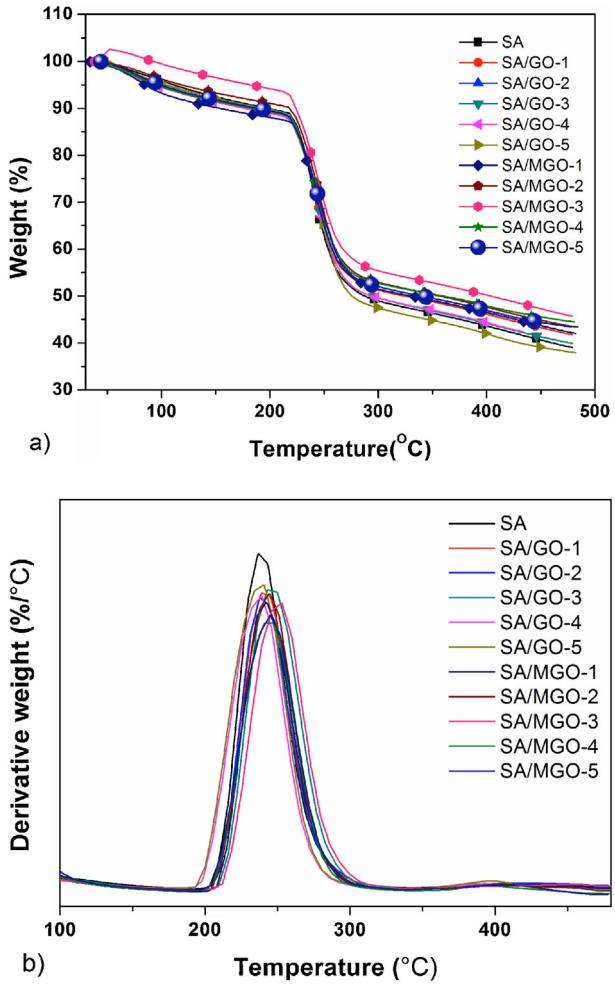

Fig. 5. *TG* (a) and *DTG* (b) curves of *SA*, *SA/GO-n* and *SA/MGO-n* biocomposite films.

was observed, which contributed to the well dispersion resulting from the strong interaction between *GO* and *SA*. For the *SA/MGO-1*, *SA/MGO-3* (Fig. 6c and e), the *MGO* was better dispersed in the *SA* matrix, which resulted from the stronger interactions and interfacial adhesion between *MGO* and *SA*. These results indicated that the amino groups of *MGO* are favor to dispersion of fillers. As it could be seen from Fig. 5f and g, high content of fillers were easily agglomerated, and *GO* was more serious than *MGO*. This could explain why the mechanical properties became worse when the fillers loading

Table 1
Thermal properties of neat *SA*, *SA/GO-n* and *SA/MGO-n* biocomposite films.

Sample	IDT (°C)[a]	FDT (°C)[b]	$T_{.50\%}$ (°C)[c]	T_{max} (°C)[d]
SA	200	310	287	239
SA/GO-1	201	312	322	242
SA/GO-2	202	315	356	241
SA/GO-3	203	322	359	246
SA/GO-4	200	317	296	244
SA/GO-5	201	312	278	243
SA/MGO-1	202	313	330	245
SA/MGO-2	203	317	359	247
SA/MGO-3	207	325	406	255
SA/MGO-4	205	319	362	250
SA/MGO-5	202	312	343	248

[a] The initial decomposed temperature.
[b] The final decomposed temperature.
[c] The temperature at 50% weight loss.
[d] The temperature at the maximum rate of mass loss.

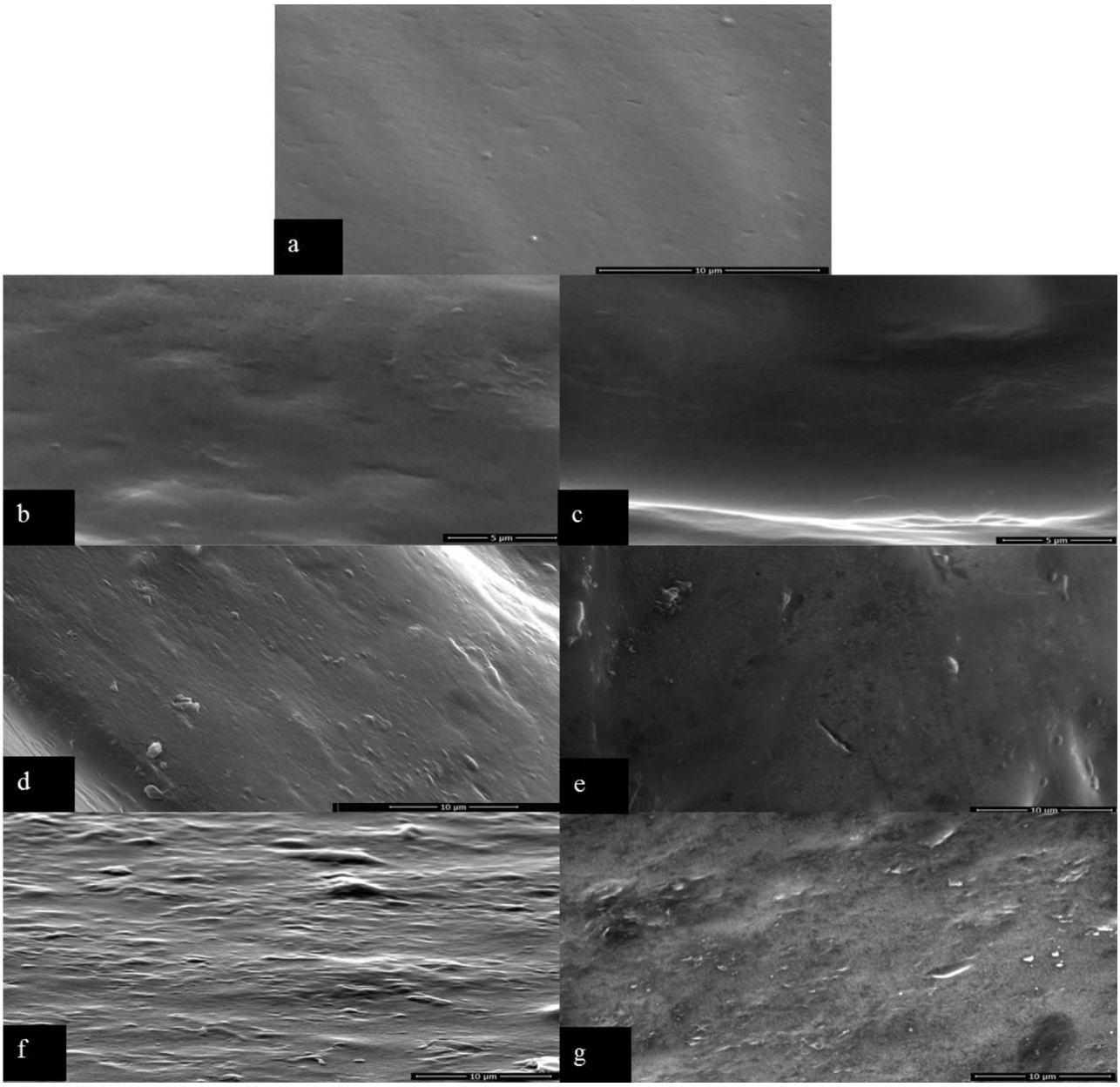

Fig. 6. *SEM* images of the fracture surfaces for neat *SA* and the *SA/GO-1*, *SA/GO-3*, *SA/GO-5*, *SA/MGO-1*, *SA/MGO-3* and *SA/MGO-5* biocomposite films.

was more than 1.0 wt%, and the mechanical properties of *SA/MGO-n* were better than that of *SA/GO-n*.

3.7. Moisture uptake of the film

The moisture uptake (*Mu*) at equilibrium at 92% RH is plotted in Fig. 7 for the biocomposite films with *GO* or *MGO*. It was found that the *Mu* value of neat *SA* film in this condition was 90.75%, indicating that moisture is absorbed by the hydrophilic biopolymer as well as voids and micro-gaps at the interface. Moreover, moisture absorption of the both biocomposite films become much lower as the *GO* or *MGO* was incorporated and showed the lowest *Mu* value when the filler loading reached 1.0 wt%. These results indicated that the addition of *GO* or *MGO* effectively decreased the *Mu* of *SA/GO-n* or *SA/MGO-n* biocomposite films. It was owing to the fact that the *GO* or *MGO* was able to form a stronger interfacial interaction with *SA* which could obstructed and weakened the diffusion of water molecules in the material. Obviously, all of the *Mu* values of *SA/GO-n* were higher than that of *SA/MGO-n* biocomposites, which resulted from that the interfacial interactions between *GO* and *SA* were weaker than that of *MGO* and *SA*.

3.8. Transparency

Film transparency is an effective index for providing information on the size of dispersed particles in the polymer matrix. Size of particles or aggregate domains which was larger than visible wavelength would obstruct light, leading to translucent or opaque films. Fig. 8 shows the *UV–vis* percent transmittance values of film samples. It was showed that the neat *SA* film presents the highest percent of transmittance, due to the absence of light blocking particles. The UV transmittance of *SA/GO-n* and *SA/MGO-n* biocomposite films decreased with increasing filler content, this can be related to both inherent particles ultraviolet absorption and higher probability of the light scattering. However, the value of *SA/GO-n* biocomposite is much higher than *SA/MGO-n* biocomposite with the

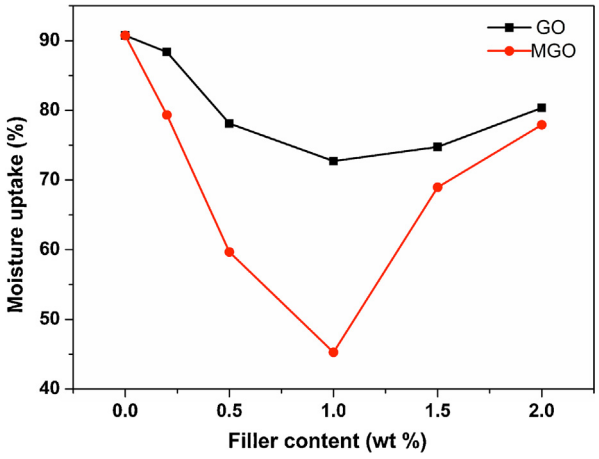

Fig. 7. The values of moisture uptake of *SA*, *SA/GO-n* and *SA/MGO-n* biocomposite films.

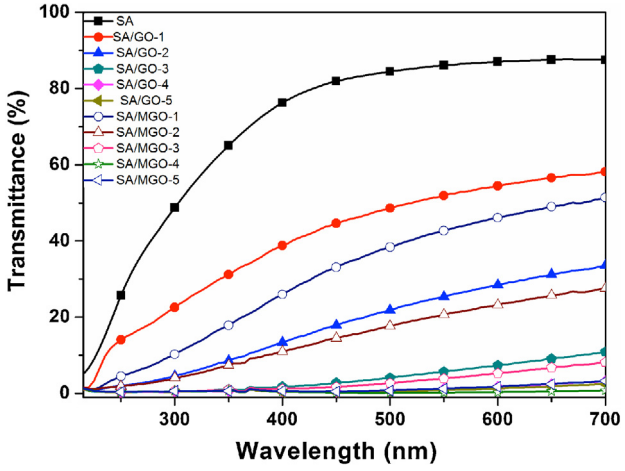

Fig. 8. *UV*–visible transmission spectra of *SA*, *SA/GO-n* and *SA/MGO-n* biocomposite films.

same loading levels. It could be concluded that the dispersibility of *MGO* was better than *GO* in the *SA* matrix, leading to less aggregate domains to obstruct the light through.

4. Conclusion

In this study, we synthesized a series of *SA/GO-n* and *SA/MGO-n* biocomposite films by a solution casting method. This investigation verified that the functional basal planes of *GO* is an effective method to improve the miscibility between *GO* and polymer. Moreover, the structures and properties of biocomposite films were strongly depended on the interfacial groups on the basal planes. *FTIR* demonstrated the hydrogen bonding interactions between the fillers and *SA*. In view of the results from tensile testing and *TGA* indicated that polymer mechanical properties and the thermal stability were improved by adding fillers, and mechanical properties and the thermal stability of *SA/MGO-n* biocomposite films were better than *SA/GO-n* biocomposite films with the same loading. Results from *SEM* showed that the fillers were dispersed well when fillers loading was lower, but the aggregations formed and *GO* was more serious than *MGO* when adding higher loading of fillers into *SA*. Results from all the experiments showed that adding active groups on the basal planes can effectively improve the properties of *SA* biocomposite films through enhancing hydrogen bonding and electrostatic interactions.

References

Augst, A. D., Kong, H. J., & Mooney, D. J. (2006). Alginate hydrogels as biomaterials. *Macromolecular Bioscience*, *6*, 623–633.

Alboofetileh, M., Rezaei, M., Hosseini, H., & Abdollahi, M. (2013). Effect of montmorillonite clay and biopolymer concentration on the physical and mechanical properties of alginate nanocomposite films. *Journal of Food Engineering*, *117*, 26–33.

Coleman, J. N., Cadek, M., Blake, R., Nicolosi, V., Ryan, K. P., & Belton, C. (2004). High-performance nanotube-reinforced plastics: Understanding the mechanism of strength increase. *Advanced Functional Materials*, *14*, 791–798.

Dreyer, D. R., Park, S., Bielawski, C. W., & Ruoff, R. S. (2010). The chemistry of graphene oxide. *Chemical Society Reviews*, *39*, 228–240.

Fayaz, A. M., Balaji, K., Girilal, M., Kalaichelvan, P. T., & Venkatesan, R. (2009). Mycobased synthesis of silver nanoparticles and their incorporation into sodium alginate films for vegetable and fruit preservation. *Journal of Agricultural and Food Chemistry*, *57*, 6246–6252.

Fang, M., Zhang, Z., Li, J., Zhang, H., Lu, H., & Yang, Y. (2010). Constructing hierarchically structured interphases for strong and tough epoxy nanocomposites by amine-rich graphene surfaces. *Journal of Materials Chemistry*, *20*, 9635–9643.

Han, D. L., Yan, L. F., Chen, W. F., & Li, W. (2011). Preparation of chitosan/graphene oxide composite film with enhanced mechanical strength in the wet state. *Carbohydrate Polymers*, *83*, 653–658.

Hummers, W. S., & Offeman, R. E. (1958). Preparation of graphitic oxide. *Journal of the American Chemical Society*, *80*, 1339.

Kawaguchi, M., Fukushima, T., Hayakawa, T., Nakashima, N., Inoue, Y., & Takeda, S. (2006). Preparation of carbon nanotube-alginate nanocomposite gel for tissue engineering. *Dental Material Journal*, *25*, 719–725.

Kim, H., Abdala, A. A., & Macosko, C. W. (2010). Graphene polymer nanocomposites. *Macromolecules*, *43*, 6515–6530.

Ma, T. T., Chang, P. R., Zheng, P. W., & Ma, X. F. (2013). The composites based on plasticized starch and graphene oxide/reduced graphene oxide. *Carbohydrate Polymers*, *94*, 63–70.

Park, S., & Ruoff, R. S. (2009). Chemical methods for the production of graphenes. *Nature Nanotechnology*, *4*, 217–224.

Qiu, S. L., Wang, C. S., Wang, Y. T., Liu, C. G., Chen, X. Y., Xie, H. F., et al. (2011). Effects of graphene oxides on the cure behaviors of a tetrafunctional epoxy resin. *Express Polymer Letters*, *5*, 809–818.

Rhim, J. W. (2004). Physical and mechanical properties of water resistant sodium alginate films. *Swiss Society of Food Science and Technology*, *37*, 323–330.

Rafiee, M. A., Rafiee, J., Wang, Z., Song, H., Yu, Z., & Koratkar, N. (2009). Enhanced mechanical properties of nanocomposites at low graphene content. *ACS Nano*, *3*, 3884–3890.

Sha, J., Xie, L. H., Ma, Y. L., Dong, S. M., & Wang, Y. (2011). Amino functional modification of graphene oxide sheets and its composite with epoxy resin. *China Plastics*, *25*, 28–33.

Sharma, S., Sanpui, P., Chattopadhyay, A., & Ghosh, S. S. (2012). Fabrication of antibacterial silver nanoparticle—sodium alginate–chitosan. *RSC Advances*, *2*, 5837–5843.

Suhas, D. P., Raghu, A. V., Jeong, H. M., & Aminabhavi, T. M. (2013). Graphene-loaded sodium alginate nanocomposite membranes with enhanced isopropanol dehydration performancevia a pervaporation technique. *RSC Advances*, *3*, 17120–17130.

Usuki, A., Hasegawa, N., & Kato, M. (2005). Polymer clay nanocomposites. *Advances in Polymer Science*, *179*, 135–195.

Wang, X., Jin, J., & Song, M. (2012). Cyanate ester resin/graphene nanocomposite: Curing dynamics and network formation. *European Polymer Journal*, *48*, 1034–1041.

Wang, J., Liu, C. H., Shuai, Y., Cui, X. Y., & Nie, L. (2014). Controlled release of anticancer drug using graphene oxide as a drug-binding effector in konjac glucomannan/sodium alginate hydrogels. *Colloids and Surfaces B*, *113*, 223–229.

Yuan, X. Y., Zou, L. L., Liao, C. C., & Dai, J. W. (2012). Improved properties of chemically modified graphene/poly(methyl methacrylate) nanocomposites via a facile in-situ bulk polymerization. *Express Polymer Letters*, *6*, 847–858.

Zhong, D., Huang, X., Yang, H., & Cheng, R. (2011). New insights into viscosity abnormality of sodium alginate aqueous solution. *Carbohydrate Polymers*, *81*, 948–952.